RESEARCH ARTICLE

National Science Open
4: 20240003, 2025
https://doi.org/10.1360/nso/20240003

Earth and Environmental Sciences

Special Topic: Nuclear Environment Advances

Selective capture of iodate anions by a cerium-based metal-organic framework

Yuting Zhao[#], Jie Li[#], Long Chen[#], Qi Guo, Lingyi Li, Linwei He, Fuwan Zhai, Mingxing Zhang, Zhifang Chai & Shuao Wang[*]

State Key Laboratory of Radiation Medicine and Protection, School of Radiation Medicine and Protection, Collaborative Innovation Center of Radiological Medicine of Jiangsu Higher Education Institutions, Soochow University, Suzhou 215123, China

#Contributed equally to this work.
*Corresponding author (email: shuaowang@suda.edu.cn)

Received 24 January 2024; Revised 19 March 2024; Accepted 13 May 2024; Published online 13 September 2024

Abstract: Effective remediation of radioactive IO_3^- is highly desirable for fuel reprocessing, medical waste disposal, and nuclear accidents. However, the nature of high solubility, strong mobility, and extremely hard to bind with minerals for IO_3^- makes this task an enormous challenge. Herein, a metal-organic framework material [Ce(IV)-MOF-808] with available Ce(IV) sites was used to efficiently remove IO_3^-. Ce(IV)-MOF-808 exhibits superior selectivity and one of the highest adsorption capacities (623 $mg \cdot g^{-1}$) for IO_3^- removal. Moreover, Ce(IV)-MOF-808 shows great adsorption performance for IO_3^- at low concentrations, and the distribution coefficient (K_d) value was calculated to be 2.60×10^6 $mL \cdot g^{-1}$. The exceptional IO_3^- uptake performance is attributed to the high affinity between Ce(IV) cluster and the oxyanion based on the comprehensive analysis of zeta potential and X-ray photoelectron spectroscopy (XPS) results, in which IO_3^- can easily replace the weakly coordinated ligand and form a strong coordination structure of Ce-O-I-O_2. More importantly, Ce(IV)-MOF-808 exhibits excellent uptake performance for IO_3^- from both the simulated Beishan groundwater system and Hanford groundwater system in the dynamic column separation test, indicating the highly promising practical application of Ce(IV)-MOF-808 in IO_3^- remediation from actual radioactive wastes.

Keywords: iodate, metal-organic framework, selectivity, distribution coefficient, adsorption

INTRODUCTION

Radioiodine is a great risk driver for human health due to its high toxicity and specific bioaccumulation in the thyroid gland [1–3]. ^{129}I is one of the most detrimental radioisotopes with a high fission yield and a long half-life (1.57×10^7 years) [4] and as a result, leads to a large inventory in nuclear wastes. However, the highly soluble and mobile nature of radioiodine in aqueous solution endows it with an extremely high risk of release during nuclear waste disposal, waste storage, or nuclear accidents. In fact, a large amount of radioiodine has been leaked into the environment in the Fukushima disaster [5] and several regions where nuclear wastes are processed or stored. For example, groundwater from the Department of Energy's Savannah River Site (SRS) is highly contaminated with ^{129}I [6]. As one kind of medical radionuclide, ^{131}I ($t_{1/2}$ = 8 d) has been well-used in

cancer diagnosis and treatment, resulting in a large quantity of medical radioiodine wastewater. With the development of nuclear medicine, there will be an increasing risk of radioiodine contamination from the growing volume of medical wastewater [7–10]. Radioiodine primarily exists in the form of iodide (I^-) and iodate (IO_3^-) in an aqueous solution. IO_3^- is the dominant species in highly aerobic conditions, which accounts for approximately 70.6% of the total iodine in the groundwater at the Hanford site [11]. Therefore, the safe and effective removal of radioactive iodate is crucial for radioactive waste management, medical waste disposal, and contaminated water remediation.

Recently, numerous works have been dedicated to the investigation of diverse iodine sorbents for the efficient removal of radioactive iodine under aqueous and/or gas environments, such as minerals [12,13], zeolites [14,15], activated carbon [16–19], and covalent organic frameworks (COFs) [20–23]. However, compared with I^-, I_2, and CH_3I, research on IO_3^- removal is seriously inadequate. Metal oxides and their composite materials [24–26], anion exchange resins [27], and layered double hydroxides (LDHs) [3,28] are the most commonly used sorbents for the separation of IO_3^-. Metal oxides and metal composites, such as Cu_2O@CH, a Cu_2O-loaded three-dimensional bulk cationic hydrogel composite exhibit excellent radiation resistance in radioiodine removal, but show poor capability and low distribution coefficient for IO_3^- (K_d = 5.33 × 10^2 mL·g^{-1}) [1]. Traditional anion exchange resins, such as Purolite A530E, show an inferior adsorption capacity for IO_3^-, and exhibit low uptake selectivity and poor radiation resistance in IO_3^- removal [27]. LDHs are a class of well-used water remediation sorbents with the merits of low cost, high adsorption capacity and good radiation resistance. However, it shows poor uptake selectivity and low K_d values for IO_3^- removal [29]. Therefore, it is of great significance to develop promising sorbents with the virtues of high uptake capacity, excellent selectivity, and high K_d values aiming at radioactive IO_3^-.

According to Pearson's theory of hard-soft-acid base (HSAB), high-valent metal ions such as Ce^{4+}, which are characterized as hard Lewis acids, show high affinity to hard Lewis bases, such as IO_3^- [30]. In addition, the extremely low solubility of $Ce(IO_3)_4$ in aqueous solution (K_{sp} = 5 × 10^{-17}) [31] reveals the strong combination between Ce(IV) and IO_3^- in aqueous solution. Therefore, Ce(IV)-based adsorbents will be promising sorbents for remediating IO_3^- contamination. However, most Ce(IV)-based sorbents, such as CeO_2, show extremely poor uptake capacity for IO_3^- remediation due to the lack of available coordination sites in the structure. Therefore, aiming to make the Ce(IV) site available, metal ions and ligands with open metal sites or weak coordination bonds are highly desirable. Metal-organic frameworks (MOFs) constructed by organic ligands bridging inorganic nodes (metal ions or clusters) are one of the most promising materials for fabricating Ce(IV)-based adsorbents with accessible Ce(IV) clusters due to the variability of ligands and coordination structures. However, the systematic design and development of MOFs with open metal sites or weak coordination bonds for the efficient removal of radioactive IO_3^- is still in its infancy.

Herein, MOFs with Ce(IV) hexanuclear clusters [Ce(IV)-MOF-808] [32] were selected for the removal of radioactive IO_3^- due to the capability to make the Ce(IV) site available through the unsaturated coordination of Ce(IV) and the weak coordination groups upon Ce(IV) (OH^- and H_2O). Ce(IV)-MOF-808 not only exhibits ultrahigh capture capacity (623 mg·g^{-1}) and superior distribution coefficient (K_d = 2.60 × 10^6 mL·g^{-1}) for IO_3^- but also shows high selectivity for IO_3^- under the condition of superabundant competing ions. More importantly, it exhibits an excellent capability for IO_3^- remediation in the simulated Beishan and Hanford groundwater system, indicating the powerful potential application of Ce(IV)-MOF-808 for the efficient removal of IO_3^- from nuclear waste liquid solutions or contaminated natural water systems.

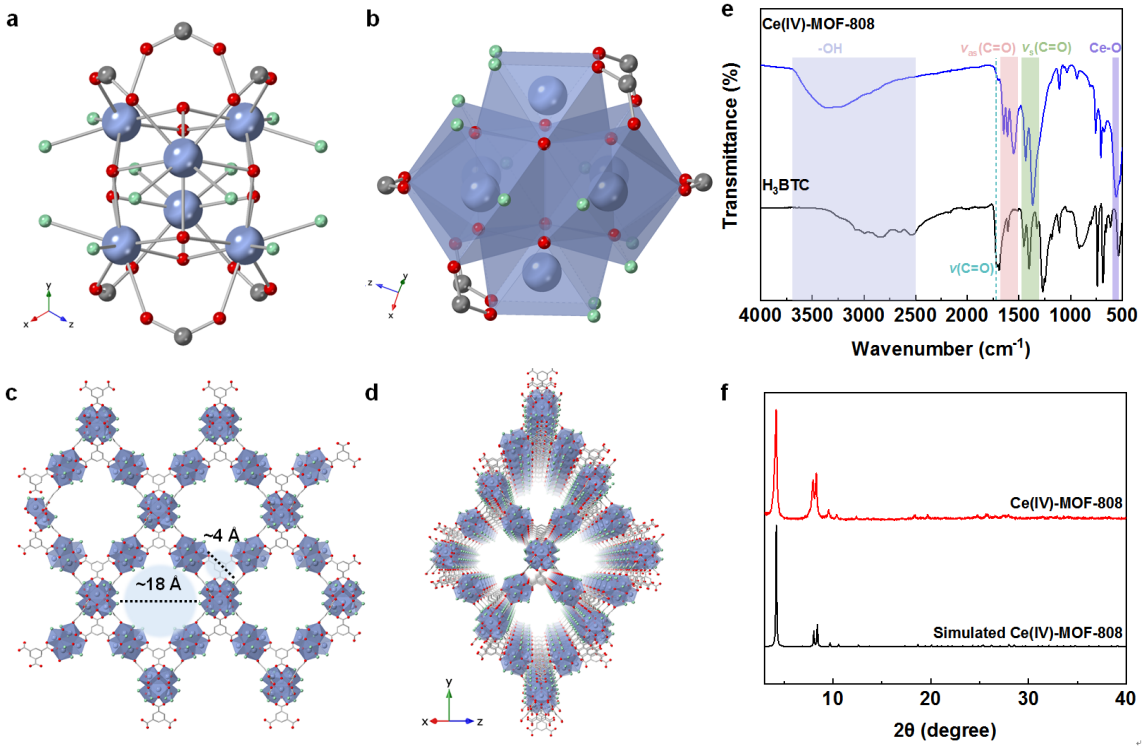

Figure 1 Crystal structure of Ce(IV)-MOF-808. Ball-and-stick model (a) and polyhedral model (b) of the Ce_6 cluster. The flat sheet (c) and 3D framework (d) of Ce(IV)-MOF-808. Atom colors: Ce = purple; C = gray; O = red; O (OH/H_2O) = green; H atoms are omitted for clarity. (e) FT-IR spectra of Ce(IV)-MOF-808 (blue) and H_3BTC (black). (f) PXRD pattern of Ce(IV)-MOF-808: simulated (black) and synthesized (red).

RESULTS AND DISCUSSION

Characterization of Ce(IV)-MOF-808

Ce(IV)-MOF-808 $[Ce_6(\mu_3\text{-}O)_4(\mu_3\text{-}OH)_4(BTC)_2(OH)_6(H_2O)_6]$ was obtained under a solvothermal reaction from a mixture of the corresponding organic ligand (H_3BTC) dissolved in DMF and an aqueous cerium ammonium nitrate solution (Figure 1a, 1b) [32]. In this structure, each $[Ce_6(\mu_3\text{-}O)_4(\mu_3\text{-}OH)_4]^{12+}$ cluster is consisted with six hydroxyl groups and six H_2O molecules through weak coordination. Ce(IV)-MOF-808 exhibits a 3,6-connected 3D framework with **spn** and tetrahedral cages of approximately 4 Å and large adamantane pores of 18 Å in diameter (Figure 1c, 1d). The crystalline structure of Ce(IV)-MOF-808 was characterized by Fourier transform infrared (FT-IR) and Powder X-ray diffraction (PXRD). As shown in Figure 1e, the presence of a wide band range of 2500–3700 cm^{-1} in Ce(IV)-MOF-808 indicates the presence of the –OH group in the Ce(IV)-MOF-808 structure [33]. The ν(C=O) of the COOH group disappears at 1717 cm^{-1}, while ν(COO-) appears. At the same time, the ν_{as}(C=O) of ν(COO-) in Ce(IV)-MOF-808 is split into three peaks (1647 cm^{-1}, 1610 cm^{-1} and 1551 cm^{-1}) and ν_s(C=O) into two peaks (1434 cm^{-1} and 1366 cm^{-1}) [34]. The new peak at 556 cm^{-1} is caused by the tensile vibration of Ce–O in Ce(IV)-MOF-808 [35]. These results indicate the formation of a coordination bond between H_3BTC and Ce(IV). Furthermore, the PXRD pattern of synthesized Ce(IV)-MOF-808 (Figure 1f) is consistent with that of the simulated result, confirming the successful synthesis of Ce(IV)-MOF-808.

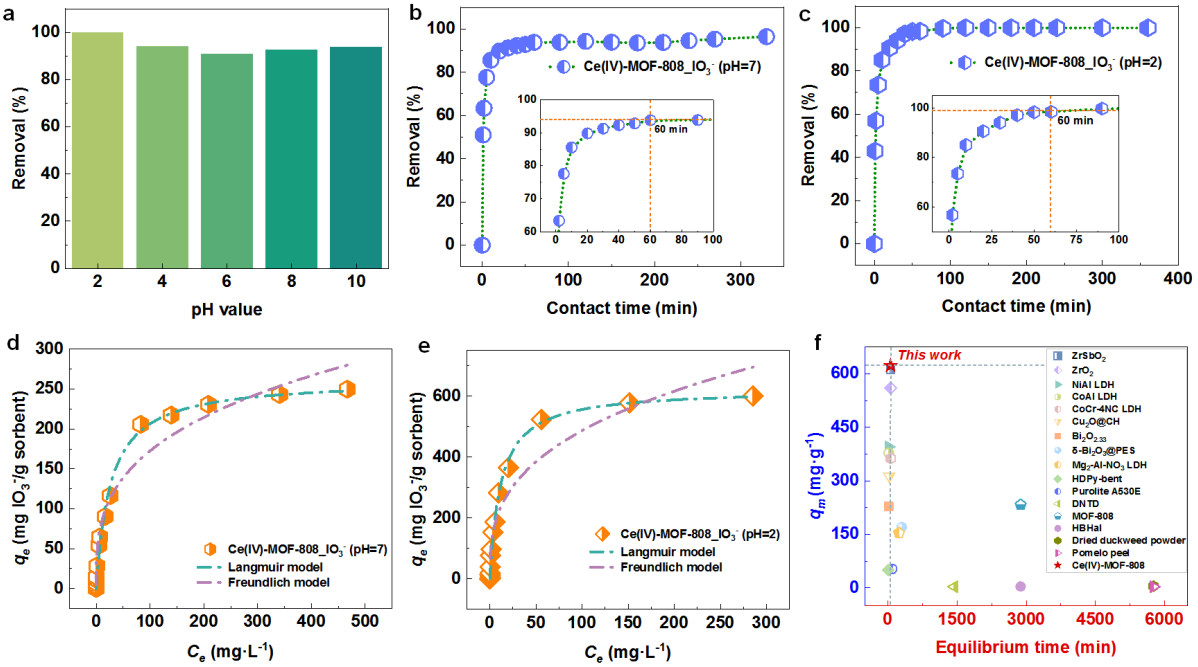

Figure 2 (a) Effect of pH value on the sorption properties of IO_3^- by Ce(IV)-MOF-808 (Conditions: contact time = 12 h, $[I]_{initial}$ = 50 mg·L^{-1}, $m_{sorbent}/V_{solution}$ = 1 g·L^{-1}). Adsorption kinetics curve under the condition of pH 7 (b) and pH 2 (c) (Conditions: $[I]_{initial}$ = 50 mg·L^{-1}, $m_{sorbent}/V_{solution}$ = 1 g·L^{-1}). Adsorption isotherm curve under the condition of pH 7 (d) and pH 2 (e) (Conditions: contact time = 12 h, $m_{sorbent}/V_{solution}$ = 1 g·L^{-1}). (f) Comparison of equilibrium time and the maximum capacity for reported adsorbents and Ce(IV)-MOF-808 in this work. The detailed experimental conditions, including the solid/liquid ratio and pH values, are listed in Table S6.

pH effect analysis

Considering the high concentration of H^+/OH^- in radioactive waste, the influence of different pH conditions on the adsorption of IO_3^- by Ce(IV)-MOF-808 was first investigated. As shown in Figure 2a, the uptake percentage of IO_3^- by Ce(IV)-MOF-808 shows negligible changes and over 95% of IO_3^- can be removed in the range of pH 4–10. Besides, when the pH value changed to 2, the removal of IO_3^- obviously increased and nearly 99% of IO_3^- was removed. To further explore the relation between pH and adsorption behavior, the zeta potential of Ce(IV)-MOF-808 was measured. As shown in Figure S2, Ce(IV)-MOF-808 exhibits positive charge under acidic conditions (pH < 7.6) and shows a strong attraction toward IO_3^- through electrostatic interactions. Besides, the high uptake capability of Ce(IV)-MOF-808 for IO_3^- removal is likely attributed to the vast –OH sites on the surface of the material that can be exchanged with IO_3^- (Ce-OH + IO_3^- → Ce-O-I-O_2 + OH^-), leading to a high capture rate of IO_3^-. Therefore, the subsequent batch experiments (except the related experiments of simulated waste liquid) explored the adsorption effect of Ce(IV)-MOF-808 on IO_3^- solutions at unregulated pH (pH~7) and pH 2, respectively.

Sorption kinetics analysis

The sorption kinetics analysis of Ce(IV)-MOF-808 for IO_3^- was studied in neutral and acidic solutions (pH 2). Ce(IV)-MOF-808 was mixed with IO_3^- solution (pH 7 or pH 2) at a solid-liquid ratio of 1 g·L^{-1} and

stirred at room temperature. IO_3^- was converted to I_3^- at 2% KI and 0.1 M H_3PO_4 (Figures S3, S4) [27], and the concentration of IO_3^- in aqueous solution was monitored by the characteristic absorption peak of I_3^- in the UV-Vis spectrum at 350 nm (Figure S5). The characteristic peak of I_3^- at 350 nm in the UV absorption spectrum disappeared at 60 min in both neutral and acidic solutions, indicating that Ce(IV)-MOF-808 can reach adsorption equilibrium (pH 7, > 93%; pH 2, > 98%) within 60 min (Figure 2b, 2c). This rapid adsorption kinetics may be attributed to the accessible and replaceable hydroxyl sites in Ce(IV)-MOF-808 [36]. The kinetics of Ce(IV)-MOF-808 for IO_3^- is faster than most of the previously reported materials, e.g., dried duckweed powder (5760 min) [37], DNTD (1440 min) [38], and pomelo peel (5760 min) [39]. In addition, pseudo-first-order and pseudo-second-order kinetic models were used to fit the adsorption processes in both environments. As shown in Table S3, the kinetics data is in line with the pseudo-second-order kinetic model, indicating that the uptake of IO_3^- on Ce(IV)-MOF-808 is accord with the chemisorption process (Figure S6). Additionally, the distribution coefficient (K_d) of Ce(IV)-MOF-808 toward IO_3^- reaches as high as 2.60×10^6 mL·g^{-1} (Table S4), indicating the powerful applications of Ce(IV)-MOF-808 in practical IO_3^- remediation.

Sorption isotherm analysis

The adsorption capacity of Ce(IV)-MOF-808 toward IO_3^- was further evaluated by adding Ce(IV)-MOF-808 to a series of IO_3^- solutions with initial concentrations ranging from 0 to 750 mg·L^{-1} (pH 7 or pH 2), and the adsorption isotherm curve was fitted by the Freundlich and Langmuir models (Figure 2d, 2e). The adsorption curve plotted by the equilibrium concentration and adsorption capacities conform to the Langmuir model. The saturated adsorption capacities for pH 7 and pH 2 were calculated to be 361 mg·g^{-1} and 623 mg·g^{-1}, respectively (Table S5). More importantly, the adsorption capacity at pH 2 is slightly higher than the reported highest capacity ($ZrSbO_2$: 612.5 mg·g^{-1}) [40], setting a new record in adsorption capacity towards IO_3^-. The high adsorption capacity under acidic conditions is attributed to the positively charged surface of Ce(IV)-MOF-808 under acidic conditions which introduces more adsorption sites into Ce(IV)-MOF-808 based on electrostatic interactions. In fact, this capacity is significantly higher than most of previously reported adsorbents, including oxide composites (Cu_2O@CH, 313.4 mg·g^{-1}) [1], natural materials (dried duckweed powder, 5.1 mg·g^{-1}) [38], resins (Purolite A530E, 53.3 mg·g^{-1}) [27], naturally occurring porous minerals (HDPy-bent, 50.2 mg·g^{-1}) [41], and LDHs (NiAl LDH, 395.5 mg·g^{-1}) [29] (Figure 2f and Table S6). This result indicates that Ce(IV)-MOF-808 may be a promising candidate for practical IO_3^- remediation from nuclear waste with the virtue of generating less amount of secondary radioactive waste.

Selectivity

Since competing anions, such as SO_4^{2-}, NO_3^-, and Cl^-, often excessively coexist with IO_3^- in the radioactive waste solutions. The uptake selectivity of Ce(IV)-MOF-808 for IO_3^- was studied under the condition of different concentrations of competing anions. As shown in Figure 3a, the removal rate of IO_3^- shows negligible changes as the concentrations of NO_3^- or Cl^- increased under the condition of pH 7. When the concentration of NO_3^- and Cl^- increases to 100 times than that of IO_3^-, the removal rates of IO_3^- by Ce(IV)-MOF-808 remain above 92.1% and 91.8%, respectively. Meanwhile, Ce(IV)-MOF-808 shows the same trend

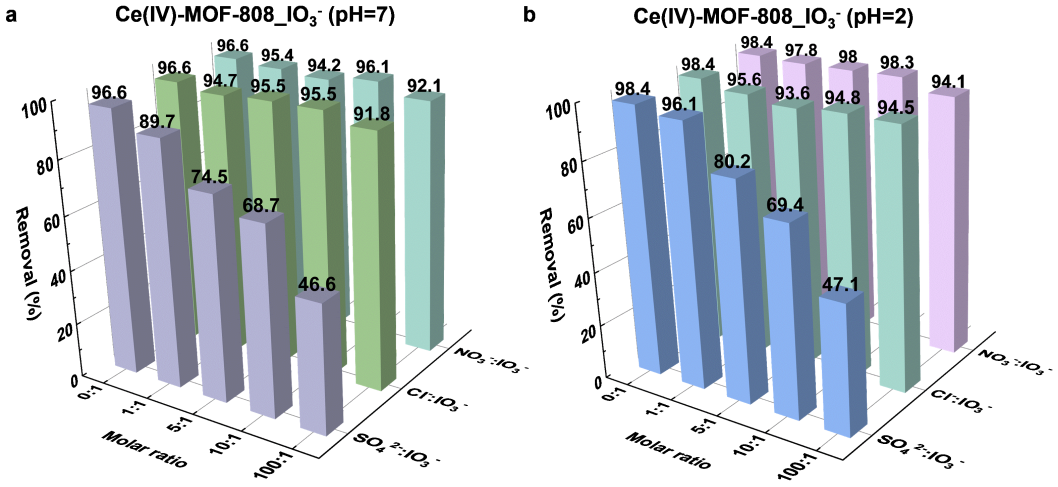

Figure 3 Effect of competing anions on the removal percentage of IO_3^- by Ce(IV)-MOF-808 under the condition of pH 7 (a) and pH 2 (b). Conditions: contact time = 12 h, $[I]_{initial}$ = 20 mg·L^{-1}, $m_{sorbent}/V_{solution}$ = 1 g·L^{-1}.

on IO_3^- removal under the condition of pH 2 that 94% of IO_3^- is removed under 100 times excess of both NO_3^- and Cl^-, indicating the excellent uptake selectivity of Ce(IV)-MOF-808 for IO_3^- removal (Figure 3b). Moreover, anions (SO_4^{2-}) with higher charge density usually have greater competition than lower charge density anions IO_3^- according to the anti-Hofmeister bias [42]. However, Ce(IV)-MOF-808 can still remove 46.6% and 47.1% of IO_3^- when the molar ratio of SO_4^{2-} to IO_3^- is as high as 100: 1 under the condition of pH 7 and pH 2, respectively. This excellent uptake selectivity of Ce(IV)-MOF-808 for IO_3^- makes it a promising candidate to selectively remove IO_3^- from wastes with high ionic strengths.

Radiation stability

Considering the high radioactivity of nuclear wastes, the radiation resistance of Ce(IV)-MOF-808 was evaluated by comparing the FT-IR spectrum, PXRD pattern and adsorption capacity of Ce(IV)-MOF-808 before and after irradiation. As shown in Figure S7, the FT-IR spectrum and the PXRD pattern of Ce(IV)-MOF-808 remain almost unchanged after being irradiated for different doses, showing that the structure of Ce(IV)-MOF-808 remains stable under irradiation. In addition, Ce(IV)-MOF-808 shows a high uptake capacity for IO_3^- after undergoing an extremely high dose of β-ray irradiation (200 kGy) as the original sample (Figure 4a, 4b). These results indicate the outstanding radiation resistance of Ce(IV)-MOF-808.

IO_3^- removal from simulated nuclear wastes

To further explore the practical application of Ce(IV)-MOF-808 in the treatment of radioactive waste, we analyzed the capture capacity of Ce(IV)-MOF-808 towards IO_3^- in the simulated groundwater at the Hanford site in the United States and the Beishan high-level waste disposal site in China. As shown in Table S1, high amounts of competing ions coexist in the simulated wastes. For example, the amounts of Cl^- and SO_4^{2-} far exceed than that of IO_3^- by more than 1200 times in the simulated BGW (Table S2), which presents a huge challenge for the selective removal of IO_3^-. Exhilaratingly, over 99% IO_3^- in both simulated systems was

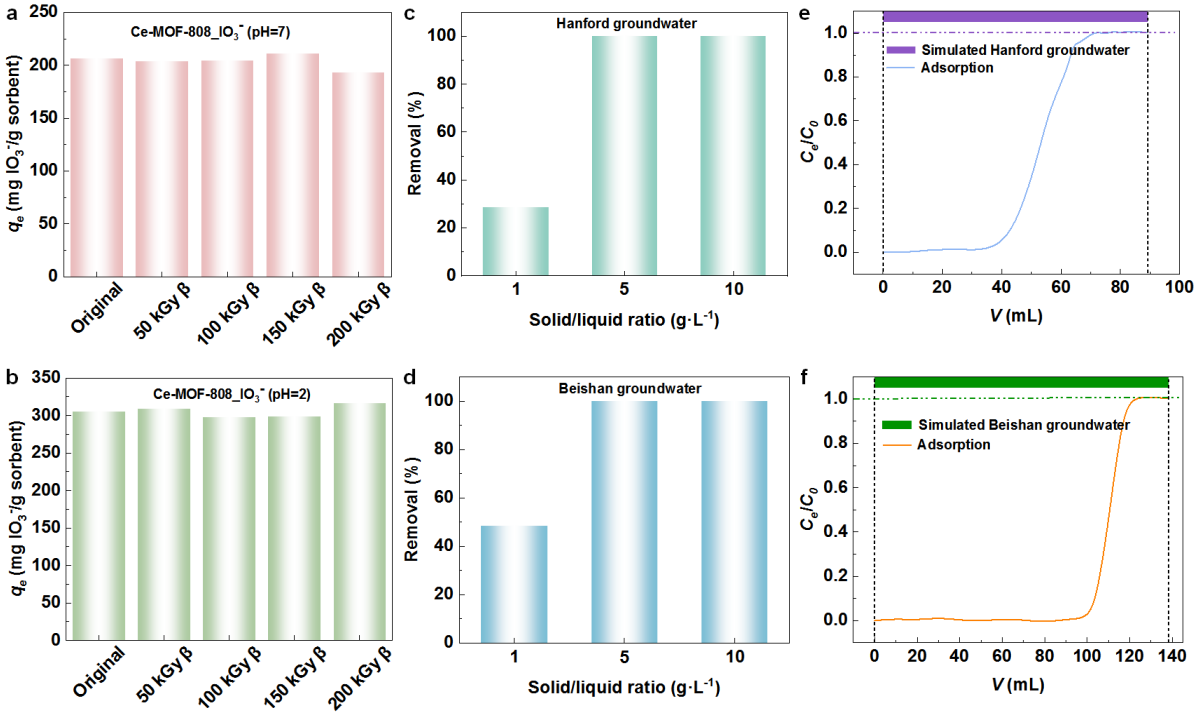

Figure 4 The removal percentage of IO_3^- under the condition of pH 7 (a) and pH 2 (b) after β irradiation compared with the original Ce (IV)-MOF-808 sample (Conditions: contact time = 12 h, $[I]_{initial}$ = 200 mg·L^{-1}, $m_{sorbent}/V_{solution}$ = 1 g·L^{-1}). The removal percentage of IO_3^- by Ce (IV)-MOF-808 from the simulated Hanford groundwater (c) and Beishan groundwater (d) (Conditions: contact time = 12 h, $[I]_{initial}$ = 1 mg·L^{-1}). Dynamic adsorption curve of Ce(IV)-MOF-808-packed column for IO_3^- capture from the simulated Hanford groundwater (e) and Beishan groundwater (f) (Conditions: $[I]_{initial}$ = 1 mg·L^{-1}, $m_{sorbent}$ = 200 mg, flow rate = 0.15 mL·min^{-1}).

removed by Ce(IV)-MOF-808 with a solid/liquid ratio of 5 g·L^{-1} (Figure 4c, 4d and Table S7). These results show the bright practical application of Ce(IV)-MOF-808 in IO_3^- remediation from actual radioactive waste.

Dynamic column separation

To further validate the potential of Ce(IV)-MOF-808 in practical scenarios, we evaluated the uptake performance of Ce(IV)-MOF-808 via a dynamic column breakthrough experiment. Ce(IV)-MOF-808 (200 mg) was packed in a plastic column with an inner diameter of 12.5 mm and further connected to the peristaltic pump for the dynamic column experiment (Figure S8). The flow rate of the simulated HGW or BGW solution was set to 0.15 mL·min^{-1} through the control system. As shown in Figure 4e, almost complete adsorption of IO_3^- by Ce(IV)-MOF-808 is observed within the initial 40 mL in the simulated HGW. Then, the concentrations of IO_3^- in the effluent increased continuously, hinting that the adsorption sites were gradually occupied by IO_3^- and the remaining adsorption sites gradually decreased during this period. The dynamic adsorption process reached equilibrium after being carried out with ~72 mL of IO_3^- stock solution, and the effluent concentration (C_e) was very close to that of the stock solution (C_0). Similarly, for the simulated BGW (Figure 4f), Ce(IV)-MOF-808 could almost completely adsorb IO_3^- within the initial 100 mL and reached equilibrium after being carried out with 120 mL of IO_3^- stock solution. The above results show that Ce(IV)-MOF-808 exhibits excellent uptake selectivity for IO_3^- and is highly desirable for actual IO_3^- separation from

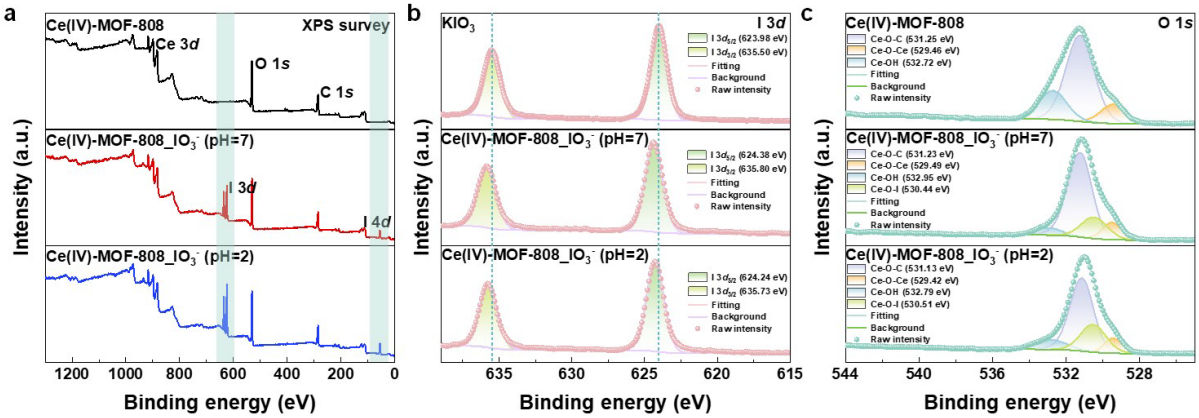

Figure 5 XPS spectra of Ce(IV)-MOF-808 before and after IO_3^- adsorption. (a) Full survey XPS spectra. (b) I 3*d* of Ce(IV)-MOF-808 before and after adsorption. (c) O 1*s* of Ce(IV)-MOF-808 before and after adsorption.

radioactive wastes.

Investigation of the adsorption mechanism

To further explore the adsorption mechanism, the structure of Ce(IV)-MOF-808 before and after IO_3^- adsorption was characterized by energy-dispersive X-ray spectroscopy (EDS) mapping, FT-IR spectroscopy, and X-ray photoelectron spectroscopy (XPS). In the EDS mapping of Ce(IV)-MOF-808_IO_3^-, the uniform distribution of element I indicates its homogeneous adsorption (Figures S9 and S10). The FT-IR spectra of Ce (IV)-MOF-808 before and after IO_3^- adsorption were collected in the range of 4000–500 cm^{-1} (Figure S11). The characteristic peak of –OH on Ce(IV)-MOF-808 decreased significantly after adsorption, indicating that the excellent IO_3^- uptake capability possibly originates from the replacement of –OH. The changes of surface elements and interaction mechanism before and after Ce(IV)-MOF-808 adsorption IO_3^- were analyzed by XPS (Figure 5). As shown in Figure 5a, new peaks identified at 624 and 54 eV in full XPS spectra appear after adsorption of IO_3^- and correspond to the characteristics of I 3*d* orbitals and I 4*d* orbitals, respectively [43]. This result indicates that IO_3^- is successfully captured onto Ce(IV)-MOF-808. Meanwhile, I $3d_{3/2}$ (pH = 7, 635.80 eV; pH = 2, 635.73 eV) and I $3d_{5/2}$ (pH = 7, 624.38 eV; pH = 2, 624.24 eV) in the I 3*d* spectra after adsorption (Figure 5b) also confirm the above conclusion.

The I 3*d* and O 1*s* spectra were widened and studied in detail to obtain a better understanding of the adsorption mechanism. The binding energies of I $3d_{3/2}$ and I $3d_{5/2}$ in Ce(IV)-MOF-808 after adsorption are shifted toward higher binding energies compared to KIO_3 (Figure 5b), suggesting that the electron cloud density around I decreases after adsorption, likely because of the reduction of electrons given to I by O in IO_3^- after adsorption caused by the formation of strong coordination between O in IO_3^- and Ce in Ce(IV)-MOF-808.

The O 1*s* spectrum of the original Ce(IV)-MOF-808 can be divided into three peaks at 532.72, 531.25, and 529.46 eV, which were associated with Ce-OH, Ce-O-C, and Ce-O-Ce, respectively (Figure 5c). The peak of Ce-OH on Ce(IV)-MOF-808 decreases obviously after adsorption compared with that of the original Ce(IV)-MOF-808, accompanied by the new peaks of Ce-O-I [530.44 eV (pH = 7) and 530.51 eV (pH = 2)] caused by

the coordination between O in IO_3^- and Ce in Ce(IV)-MOF-808. This result illustrates that the weak coordination functional group, –OH, is replaced by IO_3^- in the adsorption process and forms a strong coordination between IO_3^- and Ce in Ce(IV)-MOF-808. Therefore, combined with the XPS result of I 3*d*, the adsorption mechanism can function as following equation:

$$\text{Ce-OH} + IO_3^- \rightarrow \text{Ce-O-I-O}_2 + OH^- \quad (1)$$

Besides, the peak area of Ce-O-I adsorbed in the acidic environment (22.68%) is larger than that of Ce-O-I in the neutral environment (19.55%). This is due to high hydroxyl protonation on the surface of Ce(IV)-MOF-808 under acidic conditions, making the formation of Ce-O-I easier. This result is consistent with the bath adsorption results that the adsorption capacity of Ce(IV)-MOF-808 for IO_3^- in the acidic environment is higher than that in the neutral environment.

CONCLUSIONS

In summary, Ce(IV)-MOF-808 exhibits excellent adsorption properties toward IO_3^- removal including fast adsorption kinetics, ultrahigh adsorption capacity (623 $mg \cdot g^{-1}$), excellent selectivity, and high K_d value. Moreover, superior IO_3^- remediation is achieved both in static adsorption and dynamic column breakthrough from the simulated Hanford groundwater and Beishan groundwater, coupled with decent radiation resistance, endowing Ce(IV)-MOF-808 with promising application prospects in practical scenarios. The XPS results demonstrate that the excellent adsorption performance of Ce(IV)-MOF-808 is attributed to the high affinity between IO_3^- and Ce that the weakly coordinated hydroxyl groups in Ce(IV)-MOF-808 can be easily replaced by IO_3^-, leading to the strongly coordinated Ce-O-I between IO_3^- and Ce. This work not only reports a promising candidate for IO_3^- remediation from complex radioactive water systems, but also highlights new opportunities for the rational design of promising adsorbent materials for efficient removal of IO_3^-.

EXPERIMENTAL

Materials and reagents

Cerium ammonium nitrate [$(NH_4)_2Ce(NO_3)_6$, purity > 99.0%] was supplied by Shanghai Macklin Biochemical Technology Co., Ltd. 1,3,5-Benzenetricarboxylic acid (H_3BTC, purity > 99.0%) and potassium iodate (KIO_3, purity > 99.0%) were purchased from Shanghai Titan Scientific Co., Ltd. N, N-Dimethylformamide (DMF) was supplied by Jiangsu Qiangsheng Functional Chemical Co., Ltd. Formic acid (HCOOH) was purchased from Sinopharm Chemical Reagent Co., Ltd. Acetone (CH_3COCH_3) was supplied by Shanghai Lingfeng Chemical Reagent Co., Ltd. NaCl, $NaNO_3$, Na_2SO_4, HCl, NaOH, H_3PO_4, KI and other reagents were purchased and used from suppliers in analytically pure form.

Synthesis of Ce(IV)-MOF-808

Ce(IV)-MOF-808 was synthesized based on previous reports [32]. Ce(IV)-MOF-808 was prepared by a solvothermal method, as shown in Scheme S1. H_3BTC (22.4 mg, 106 μmol), $(NH_4)_2Ce(NO_3)_6$ (175.3 mg,

318 μmol), H_2O (0.6 mL), DMF (1.2 mL) and HCOOH (257 μL) were successively added to a 10 mL scintillation bottle, and heated at 100°C on an oil bath magnetic stirring heater for 15 min. The products were separated by centrifugation, washed with DMF (2 mL × 2) and acetone (2 mL × 4), and dried at 70°C for 2 h to obtain a light yellow solid (Figure S1).

Characterizations

The β irradiation of materials was performed using the electron irradiation accelerator device of Shanghai Institute of Applied Physics (1.5 MeV; 1.4 mA; 80 kW). Scanning electron microscopy (SEM) images and energy dispersive X-ray spectroscopy (EDS) were obtained by an EVO 18 scanning electron microscope from Carl Zeiss, Germany. Fourier transform infrared (FT-IR) spectra in the range of 4000–400 cm^{-1} were recorded by a Thermo Nicolet iS50 conventional Fourier infrared spectrometer (USA). Power X-ray diffraction (PXRD) datas were collected at 2θ from 3° to 40° with a step of 0.02° by D8 Advance X-ray powder diffraction instrument in Bruker, Germany (Cu Kα rays (λ = 1.54056 Å; 40 kV; 40 mA)). The zeta potential was measured with Malvern Zetasizer Nano ZS90 (UK). X-ray photoelectron spectroscopy (XPS) spectra were measured using Thermo Scientific ESCALAB Xi+ (USA). A monochromatic Al Kα source (Mono Al Kα) with an energy of 1486.6 eV was used as the excitation source. The data were fitted and analyzed by Avantage XPS software, and the binding energies were calibrated through C 1*s* hydrocarbon peak at 284.8 eV. The concentrations of IO_3^- in the solution were determined by monitoring the characteristic absorption peak of I_3^- derived from IO_3^- at 350 nm by a UV-2600 Vis-spectrometer in Shimadzu, Japan.

Batch experiments

All adsorption experiments were performed at 25°C by using the batch adsorption method. Typically, Ce (IV)-MOF-808 (5 mg) was placed into aqueous solution containing certain contents of IO_3^- (5 mL). The pH was adjusted with diverse concentrations of NaOH and/or HCl solutions. After stirring the mixture on a magnetic mixer at 300 $r \cdot min^{-1}$ for desired adsorption time, the solid-liquid phase was separated with a 0.22 μm nylon membrane filter (SANJIA Biochemical Supplies). Taking into account the phenomenon that IO_3^- has no UV characteristic absorption peak in UV-Vis spectrum, the concentration of IO_3^- was measured by the characteristic peak of I_3^- at 350 nm based on the reaction that IO_3^- is converted into I_3^- after mixing 2 mL of sample with 1 mL of 0.1 M H_3PO_4 solution and 1 mL of 2% KI solution. In an acidic solution containing excess I^-, IO_3^- reacts with I^- and converts to elemental iodine, which then interacts with I^- to form I_3^- [44]. The specific reactions are as follows:

$$IO_3^- + 5I^- + 6H^+ \rightarrow 3I_2 + 3H_2O \quad (2)$$

$$I_2 + I^- \rightarrow I_3^- \quad (3)$$

$$IO_3^- + 8I^- + 6H^+ \rightarrow 3I_3^- + 3H_2O \quad (4)$$

The removal percentage (η) and sorption amount (q_e) of Ce(IV)-MOF-808 for IO_3^- were calculated by the following formulas:

$$\eta = \frac{C_0 - C_e}{C_e} \times 100\% \quad (5)$$

$$q_e = \frac{(C_0 - C_e)V}{m} \tag{6}$$

where C_0 (mg·L^{-1}) is the initial concentration of IO_3^- in solution; C_e (mg·L^{-1}) is the residual concentration of IO_3^- after adsorption; V (mL) and m (mg) are the volume of IO_3^- solution and the mass of Ce(IV)-MOF-808, respectively.

Effect of pH study

The pH values were adjusted by adding negligible volumes of HCl and/or NaOH solutions. Ce(IV)-MOF-808 (5 mg) was added to IO_3^- aqueous solution (5 mL, 50 mg·L^{-1}) at different pH values (2 to 10). The suspension was separated with a 0.22 μm nylon membrane filter after being stirred for 6 h, and the concentration of IO_3^- in aqueous solution was measured by a UV-Vis spectrometer.

Sorption kinetics study

The kinetics experiments were performed at pH 7 or pH 2 with a solid/liquid ratio of 1 g·L^{-1}. Typically, Ce(IV)-MOF-808 (100 mg) was added to IO_3^- solution (100 mL, 50 mg·L^{-1}). After being stirred for a certain time (0, 1, 2, 5, 10, 20, 30, 40, 50, 60, 90, 120, 150, 180, 210, 240, 270, and 330 min), the liquid phase was separated with a 0.22 μm nylon membrane filter and the concentration of IO_3^- was analyzed by a UV-Vis spectrometer.

Two kinetic models, pseudo-first-order (PFO) and pseudo-second-order (PSO) models, were used to fit the kinetics data. The linearized forms of the two models are as follows [45]:

Pseudo-first-order model:

$$\ln(q_e - q_t) = \ln q_e - k_1 t \tag{7}$$

Pseudo-second-order model:

$$\frac{t}{q_t} = \frac{1}{k_2 q_e^2} + \frac{t}{q_e} \tag{8}$$

where q_e (mg·g^{-1}) and q_t (mg·g^{-1}) are the sorption amount at equilibrium time and time t (min), respectively; k_1 (min^{-1}) and k_2 (g·mg^{-1}·min^{-1}) are the kinetic rate constants of PFO and PSO, respectively. The linearized plot of PFO and PSO was obtained when we plotted ln(q_e - q_t) and t/q_t against t, respectively.

The distribution coefficient (K_d) of Ce(IV)-MOF-808 toward IO_3^- was calculated by the following equation:

$$K_d = \frac{(C_0 - C_e)V}{mC_e} \tag{9}$$

Sorption isotherm study

The sorption isotherm experiments of Ce(IV)-MOF-808 were carried out by varying the initial IO_3^- concentrations from 0 to 750 mg·L^{-1}. In each sample, Ce(IV)-MOF-808 (5 mg) was added into IO_3^- aqueous solution (5 mL) under the condition of pH 7 or pH 2 with a solid/liquid ratio of 1 g·L^{-1}. After being stirred for 6 h, the suspension liquid was separated and the concentration of IO_3^- was measured by a UV-Vis spec-

trometer.

Two isotherm models, the Freundlich and Langmuir isotherm models were used to fit the sorption process. The Freundlich equation is based on the empirical equation for heterogeneous surface adsorption. The stronger binding sites are occupied first, and the binding strengths are gradually decreased as the occupation of the active sites. The Freundlich isotherm model is expressed in the following equations:

$$\ln q_e = \ln K_F + \frac{1}{n}\ln C_e \tag{10}$$

where K_F ($(mg \cdot g^{-1}) \times (L^{1/n} \cdot mg^{-1/n})$) and n are the Freundlich constants corresponding to the sorption capacity and strength, respectively. The linearized plot was obtained by plotting $\ln q_e$ against $\ln C_e$, and K_F and n could be calculated from the slope and intercept.

The Langmuir isotherm model assumes that the sorption process is based on monolayer and that all sites are equal. The linear equation of the Langmuir isotherm model is expressed as follows [46]:

$$\frac{C_e}{q_e} = \frac{1}{q_m K_L} + \frac{C_e}{q_m} \tag{11}$$

where q_m ($mg \cdot g^{-1}$) is the maximum sorption amount of IO_3^- corresponding to complete monolayer coverage; K_L ($L \cdot mg^{-1}$) is a constant related to the sorption capacity and energy of sorption, which characterizes the affinity of the adsorbate with the adsorbent. The linearized plot was obtained when we plotted C_e/q_e against C_e, and q_m and K_L could be calculated from the slope and intercept.

Anion selectivity study

The effects of competing anions, including NO_3^-, SO_4^{2-}, and Cl^-, were determined by adding different concentrations of $NaNO_3$, Na_2SO_4, or NaCl solutions (0.157 mM, 0.785 mM, 1.57 mM, and 15.7 mM) into a 0.157 mM IO_3^- solution. Ce(IV)-MOF-808 (5 mg) was added to the above solution (5 mL) under the condition of pH 7 or pH 2. The suspension was separated after being stirred for 6 h, and the concentration of IO_3^-, after sorption in aqueous solution was measured by a UV-Vis spectrometer.

Radiation resistance measurements

The β irradiation experiment was conducted using an electron beam by an electron accelerator. Ce(IV)-MOF-808 powder was exposed to β-irradiation for four doses (50, 100, 150, and 200 kGy). The anti-irradiation property of Ce(IV)-MOF-808 was characterized by FT-IR and PXRD spectroscopy, while the irradiated samples were further subjected to IO_3^- adsorption experiments (pH 7 or pH 2) to determine the irradiation stability of Ce(IV)-MOF-808.

Removal of IO_3^- in simulated nuclear wastes

The simulated Hanford groundwater (HGW) and Beishan groundwater (BGW) were prepared according to Table S1 and Table S2. Ce(IV)-MOF-808 (5 mg/25 mg) was added to the above simulated solutions (5 mL). The suspension was separated after being stirred for 6 h, and the concentration of IO_3^- after sorption in aqueous solution was measured by a UV-Vis spectrometer.

Dynamic column adsorption experiments

Typically, Ce(IV)-MOF-808 (200 mg) was packed in a plastic column (12.5 mm I.D.). The simulated BGW or HGW solution flowed through the column at a flow rate of 0.15 mL·min^{-1}. The concentrations of IO_3^- in the effluent were evaluated by a UV-Vis spectrometer.

Funding

This work was supported by the Intergovernmental International Cooperation of the National Key R&D Program of China (2022YFE0105300), the National Key R&D Program of China (2021YFB3200400), the National Natural Science Foundation of China (22306136, 22425061, 22176139, U2267222, and U1967217), the China National Postdoctoral Program for Innovative Talents (BX2021206), the China Postdoctoral Science Foundation (2021M702390), the Natural Science Foundation of Jiangsu (BK20230510), the New Cornerstone Science Foundation through the XPLORER PRIZE, and the Priority Academic Program Development of Jiangsu Higher Education Institutions (PAPD).

Author contributions

S.W. and Z.C. conceived and supervised the project. Y.Z. synthesized and characterized the material. Y.Z., J.L., Q.G. and L.L. performed the adsorption experiments and analyzed the data. L.H. assisted in the drawing of TOC. Y.Z. and F.Z. collected and analyzed the XPS data. M.Z. aided in the irradiation experiments. Y.Z., J.L., L.C., and S.W. wrote the paper. All authors discussed the results and commented on the manuscript.

Conflict of interest

The authors declare no conflict of interest.

Supplementary information

The supporting information is available online at https://doi.org/10.1360/nso/20240003. The supporting materials are published as submitted, without typesetting or editing. The responsibility for scientific accuracy and content remains entirely with the authors.

References

1 Yan C, Li J, Tan C, *et al.* Cuprous oxide-based cationic hydrogel by the integration of enrichment and immobilization of radioiodine (I^- , IO_3^-) in aqueous solution. *ACS Appl Mater Interfaces* 2023; **15**: 28135–28148.

2 Chen P, He X, Pang M, *et al.* Iodine capture using Zr-based metal–organic frameworks (Zr-MOFs): Adsorption performance and mechanism. *ACS Appl Mater Interfaces* 2020; **12**: 20429–20439.

3 Kang J, Levitskaia TG, Park S, *et al.* Nanostructured MgFe and CoCr layered double hydroxides for removal and sequestration of iodine anions. *Chem Eng J* 2020; **380**: 122408.

4 Asmussen RM, Westesen A, Cordova EA, *et al.* Iodine removal from carbonate-containing alkaline liquids using strong base resins, hybrid resins, and silver precipitation. *Ind Eng Chem Res* 2023; **62**: 3271–3281.

5 Mclaughlin PD, Jones B, Maher MM. An update on radioactive release and exposures after the Fukushima Dai-ichi nuclear disaster. *BJR* 2012; **85**: 1222–1225.

6 Beals DM, Hayes DW. Technetium-99, iodine-129 and tritium in the waters of the Savannah River Site. *Sci Total Environ* 1995; **173-174**: 101–115.

7 Rose PS, Smith JP, Cochran JK, *et al.* Behavior of medically-derived ^{131}I in the tidal Potomac River. *Sci Total Environ* 2013; **452-453**: 87–97.

8 Jiménez F, López R, Pardo R, *et al.* The determination and monitoring of ^{131}I activity in sewage treatment plants based

on A2/O processes. *Radiat Meas* 2011; **46**: 104–108.

9 Barquero R, Agulla MM, Ruiz A. Liquid discharges from the use of radionuclides in medicine (diagnosis). *J Environ Radioact* 2008; **99**: 1535–1538.

10 Fischer HW, Ulbrich S, Pittauerová D, *et al.* Medical radioisotopes in the environment—Following the pathway from patient to river sediment. *J Environ Radioact* 2009; **100**: 1079–1085.

11 Moore RC, Pearce CI, Morad JW, *et al.* Iodine immobilization by materials through sorption and redox-driven processes: A literature review. *Sci Total Environ* 2020; **716**: 132820.

12 Choung S, Kim M, Yang JS, *et al.* Effects of radiation and temperature on iodide sorption by surfactant-modified bentonite. *Environ Sci Technol* 2014; **48**: 9684–9691.

13 Kaplan DI, Serne RJ, Parker KE, *et al.* Iodide sorption to subsurface sediments and illitic minerals. *Environ Sci Technol* 2000; **34**: 399–405.

14 Inglezakis VJ, Satayeva A, Yagofarova A, *et al.* Surface interactions and mechanisms study on the removal of iodide from water by use of natural zeolite-based silver nanocomposites. *Nanomaterials* 2020; **10**: 1156.

15 Pham TCT, Docao S, Hwang IC, *et al.* Capture of iodine and organic iodides using silica zeolites and the semiconductor behaviour of iodine in a silica zeolite. *Energy Environ Sci* 2016; **9**: 1050–1062.

16 Ikari M, Matsui Y, Suzuki Y, *et al.* Removal of iodide from water by chlorination and subsequent adsorption on powdered activated carbon. *Water Res* 2015; **68**: 227–237.

17 Li D, Kaplan DI, Sams A, *et al.* Removal capacity and chemical speciation of groundwater iodide (I^-) and iodate (IO_3^-) sequestered by organoclays and granular activated carbon. *J Environ Radioact* 2018; **192**: 505–512.

18 Li D, Kaplan DI, Price KA, *et al.* Iodine immobilization by silver-impregnated granular activated carbon in cementitious systems. *J Environ Radioact* 2019; **208-209**: 106017.

19 Hoskins JS, Karanfil T, Serkiz SM. Removal and sequestration of iodide using silver-impregnated activated carbon. *Environ Sci Technol* 2002; **36**: 784–789.

20 Lin Y, Jiang X, Kim ST, *et al.* An elastic hydrogen-bonded cross-linked organic framework for effective iodine capture in water. *J Am Chem Soc* 2017; **139**: 7172–7175.

21 Liu X, Zhang A, Ma R, *et al.* Experimental and theoretical insights into copper phthalocyanine-based covalent organic frameworks for highly efficient radioactive iodine capture. *Chin Chem Lett* 2022; **33**: 3549–3555.

22 He L, Chen L, Dong X, *et al.* A nitrogen-rich covalent organic framework for simultaneous dynamic capture of iodine and methyl iodide. *Chem* 2021; **7**: 699–714.

23 Zhang Y, He L, Pan T, *et al.* Superior iodine uptake capacity enabled by an open metal-sulfide framework composed of three types of active sites. *CCS Chem* 2023; **5**: 1540–1548.

24 Liu S, Kang S, Wang H, *et al.* Nanosheets-built flowerlike micro/nanostructured $Bi_2O_{2.33}$ and its highly efficient iodine removal performances. *Chem Eng J* 2016; **289**: 219–230.

25 Zhao Q, Chen G, Wang Z, *et al.* Efficient removal and immobilization of radioactive iodide and iodate from aqueous solutions by bismuth-based composite beads. *Chem Eng J* 2021; **426**: 131629.

26 Wang N, Zhang G, Xiong R, *et al.* Synchronous moderate oxidation and adsorption on the surface of γ-MnO_2 for efficient iodide removal from water. *Environ Sci Technol* 2022; **56**: 9417–9427.

27 Zhao Y, Li J, Chen L, *et al.* Efficient removal of iodide/iodate from aqueous solutions by Purolite A530E resin. *J Radioanal Nucl Chem* 2023; **332**: 1193–1202.

28 Zhang D, Liu XY, Zhao HT, *et al.* Application of hydrotalcite in soil immobilization of iodate (IO_3^-). *RSC Adv* 2018; **8**: 21084–21091.

29 Kang J, Cintron-Colon F, Kim H, *et al.* Removal of iodine (I^- and IO_3^-) from aqueous solutions using CoAl and NiAl layered double hydroxides. *Chem Eng J* 2022; **430**: 132788.

30 Ho TL. Hard soft acids bases (HSAB) principle and organic-chemistry. *Chem Rev* 1975; **75**: 1–20.

31 Lide DR. CRC Handbook of Chemistry and Physics. Boca Raton: CRC Press, 2004.

32 Lammert M, Glißmann C, Reinsch H, *et al.* Synthesis and characterization of new Ce(IV)-MOFs exhibiting various

framework topologies. *Cryst Growth Des* 2017; **17**: 1125–1131.

33 Pervez MN, Chen C, Li Z, *et al.* Tuning the structure of cerium-based metal-organic frameworks for efficient removal of arsenic species: The role of organic ligands. *Chemosphere* 2022; **303**: 134934.

34 Chu L, Guo J, Huang Z, *et al.* Excellent catalytic performance over acid-treated MOF-808(Ce) for oxidative desulfurization of dibenzothiophene. *Fuel* 2023; **332**: 126012.

35 He J, Pei C, Yang Y, *et al.* The structural design and valence state control of cerium-based metal-organic frameworks for their highly efficient phosphate removal. *J Cleaner Production* 2021; **321**: 128778.

36 Jacobsen J, Ienco A, D′Amato R, *et al.* The chemistry of Ce-based metal–organic frameworks. *Dalton Trans* 2020; **49**: 16551–16586.

37 Zhang K, Chen T. Sorption and removal of iodate from aqueous solution using dried duckweed (Landoltia punctata) powder. *J Radioanal Nucl Chem* 2018; **316**: 543–551.

38 Liu P, Chen T, Zheng J. Removal of iodate from aqueous solution using diatomite/nano titanium dioxide composite as adsorbent. *J Radioanal Nucl Chem* 2020; **324**: 1179–1188.

39 Da T, Chen T. Optimization of experimental factors on iodate adsorption: A case study of pomelo peel. *J Radioanal Nucl Chem* 2020; **326**: 511–523.

40 Suorsa V, Otaki M, Virkanen J, *et al.* Pure and Sb-doped ZrO_2 for removal of IO_3^- from radioactive waste solutions. *Int J Environ Sci Technol* 2022; **19**: 5155–5166.

41 Yang J, Tai W, Wu F, *et al.* Enhanced removal of radioactive iodine anions from wastewater using modified bentonite: Experimental and theoretical study. *Chemosphere* 2022; **292**: 133401.

42 Zhang Y, Cremer PS. Chemistry of Hofmeister anions and osmolytes. *Annu Rev Phys Chem* 2010; **61**: 63–83.

43 Li J, Ma X, Zhao C, *et al.* A novel $Ce(IO_3)_4$ catalyst: Facile preparation and high activity in degradation of organic dyes without light irradiation at room temperature. *J Phys Chem Solids* 2017; **100**: 33–39.

44 Schmitz G. Kinetics and mechanism of the iodate-iodide reaction and other related reactions. *Phys Chem Chem Phys* 1999; **1**: 1909–1914.

45 Li J, Dai X, Zhu L, *et al.* $^{99}TcO_4^-$ remediation by a cationic polymeric network. *Nat Commun* 2018; **9**: 3007.

46 Langmuir I. The adsorption of gases on plane surfaces of glass, mica and platinum. *J Am Chem Soc* 1917; **40**: 1361–1403.